Mon. Not. R. Astron. Soc. **359,** 228–236 (2005) doi:10.1111/j.1365-2966.2005.08893.x

Constraining the structure of the non-spherical pre-protostellar core L1544

Steven D. Doty,[1]★ Sheila E. Everett,[1] Yancy L. Shirley,[2]†
Neal J. Evans, II[3] and Matthew L. Palotti[1,4]

[1]*Department of Physics and Astronomy, Denison University, Granville, OH 43023, USA*
[2]*National Radio Astronomy Observatory, Socorro, NM 87801, USA*
[3]*Department of Astronomy, University of Texas at Austin, Austin, TX 78712-1083, USA*
[4]*Department of Physics, University of Wisconsin–Madison, Madison, WI 53706-1390, USA*

Accepted 2005 January 28. Received 2005 January 26; in original form 2004 July 22

ABSTRACT

We present a study of the pre-protostellar core L1544. A series of self-consistent, three-dimensional continuum radiative transfer models is constructed. The outputs of these models are convolved with appropriate telescope beam responses, and compared with existing SCUBA data. The resulting comparison allows us to constrain the structure of L1544. We find that the source is well-fitted by a prolate spheroid, having an ellipsoidal power-law density distribution of index $m \sim 2 (1.75 < m < 2.25)$ in to at least $r \sim 1600$ au. For $r < 1600$ au, the data are consistent with either an extension of the power law to smaller radii, or a flattened (Bonner–Ebert-like) density distribution. Furthermore, we find an optical depth along the short axis at 1300 μm of $\tau_{1300,\mathrm{short}} = 5 \times 10^{-3} (2 \times 10^{-3} < \tau_{1300,\mathrm{short}} < 8 \times 10^{-3})$, a central luminosity $L_* = 0 (<10^{-3}\,\mathrm{L}_\odot)$, a long-axis diameter $D = 0.1$ pc $[0.08 < D(\mathrm{pc}) < 0.16; 16\,000 < D(\mathrm{au}) < 32\,000]$, an axis ratio $q = 2$ $(1.7 < q < 2.5)$, and an external interstellar radiation field (ISRF) defined by Mathis et al. to within 50 per cent. The outer diameter and axis ratio may each be somewhat larger due to potential on-source chopping in the observations, and the projection of the long axis on to the plane of the sky. While these results are similar to those inferred directly from observations or spherical modelling due to the source transparency at submillimetre wavelengths, we infer a smaller size, lower mass, and higher optical depth/column density, exposed to a stronger external radiation field than previously assumed. Finally, we find that both the spectral energy distribution (SED) and surface brightness distribution are necessary to constrain the source properties in this way, and even a modest variation in χ^2 can significantly alter the fit quality.

Key words: stars: formation – ISM: clouds – infrared: stars.

1 INTRODUCTION

The structure of bound, starless cores (e.g. Myers, Linke & Benson 1983; Benson & Myers 1989) is not well known. This structure is important, as it should drive the ensuing evolution of the core, and give insight into the initial conditions of star formation free from the disruption of a central protostar. Ward-Thompson et al. (1994) detected millimetre and submillimetre continuum radiation from dust in these regions, and dubbed them pre-protostellar cores (PPCs).

Following this detection, significant work has continued toward determining the conditions associated with these regions. Ward-Thompson et al. (1994) inferred that the density distributions do not follow isothermal sphere distributions, $n(r) \propto r^{-2}$, over a range of cores, a result supported by various other studies (e.g. André, Ward-Thompson & Motte 1996; Ward-Thompson, Motte & André 1999; Bacmann et al. 2000). These studies utilized semi-analytic techniques to infer the dust density distribution. Similar techniques such as colour temperature variation, were used by Ward-Thompson, André, & Kirk (2002) (along with *ISO* flux data) to infer the temperature distribution and to place constraints on the luminosity of the central source. While many of these semi-analytic approaches yield physically meaningful information, the specifics of the approach can affect the reliability of the conclusions (Doty & Palotti 2002).

Submillimetre (submm) data for many PPCs were obtained from the Submillimetre Common-User Bolometric Array (SCUBA) on the James Clerk Maxwell Telescope (JCMT) by Shirley et al. (2000).

★Email: doty@denison.edu
†Jansky Postdoctoral Fellow.

In an analysis of these data, Evans et al. (2001) assumed spherical symmetry and utilized a self-consistent dust radiative transfer model to infer the properties and structure of their source sample. They found that Bonner–Ebert (BE) spheres provided good fits to the data, with L1544 requiring the highest central density, $n_c = 10^6$ cm^{-3}, in fact. However, a power-law density distribution could not be ruled out when a self-consistent dust temperature variation was included. This result, while intriguing, relies upon the assumed underlying source geometry. Unfortunately, the observed isophotes for L1544 are decidedly non-spherical, leading to potential uncertainty in these conclusions.

In this paper we report on a study comparing existing data with detailed, three-dimensional, continuum radiative transfer models to constrain the conditions associated with L1544. In Section 2, we describe L1544 and previously inferred properties. We briefly describe the model and range of parameter space considered in Section 3. In Section 4, we compare the models with observations in constraining the source properties. Finally, we conclude in Section 5.

2 L1544

L1544 is located in Taurus at a distance of 140 pc (Elias 1978). The source has been well-observed. There is no reported IRAS source associated with the core (Ward-Thompson et al. 1994). However, submillimetre data have been obtained at the JCMT at 450, 850 and 1100 μm with a single element by Ward-Thompson et al. (1994), and using SCUBA (Shirley et al. 2000). Further submillimetre data were taken at 1.3 mm using IRAM (Ward-Thompson et al. 1994, 1999). L1544 has also been studied with the *Infrared Space Observatory*. In particular, Bacmann et al. (2000) utilized ISOCAM imaging data (∼7 μm), while Ward-Thompson et al. (2002) utilized the ISOPHOT photometer at 90, 170 and 200 μm.

In Table 1, we reproduce the observed fluxes that we adopt in our study. We choose the 450, 850 and 1300 μm data from Shirley et al. (2000), as the results are from an array, rather than a single-element bolometer. The 90-, 170- and 200-μm fluxes are taken from Ward-Thompson et al. (2002). In both cases, the uncertainties in Table 1 are the quoted statistical uncertainties added in quadrature with an assumed 30 per cent calibration uncertainty in the data.

The spectral energy distribution (SED) can help constrain the density distribution. However, the constraint is not unique (Butner et al. 1991; Men'shcikov & Henning 1997; Doty & Palotti 2002). On the other hand, the spatial distribution of intensity on the sky in the form of maps provides significantly more data with which to constrain the models (Adams 1991; Ladd et al. 1991). As a result, we also consider the 450- and 850-μm intensity maps produced by Shirley et al. (2000).

Table 1. Fluxes toward L1544.

Wavelength (μm)	Flux density (Jy)	Uncertainty[a]	ref
90	<0.57[b]	n/a	1
170	14.9[b]	(0.2, 4.5) = 4.5	1
200	18.6[b]	(0.3, 5.6) = 5.6	1
450	17.4[c]	(6.7, 3.5) = 7.5	2
850	3.64[c]	(0.18, 0.73) = 0.75	2
1300	0.27[d]	(0.04, 0.05) = 0.07	2

[a](Statistical, 30 per cent cal.) uncertainties added in quadrature.
[b]Flux density in a 150-arcsec aperature.
[c]Flux density in a 120-arcsec aperature.
[d]Flux density in a 40-arcsec aperature.
[1]Ward-Thompson et al. (2002).
[2]Shirley et al. (2000).

Table 2. Previously inferred conditions for L1544.

Parameter	Value	ref
Optical depth at 1300 μm (τ_{1300})	2×10^{-3}	3
Optical depth at 200 μm (τ_{200})	0.06	5
Density distribution	BE[a] or PL($m = 2$)[b]	2
ISRF ($G^c_{\rm MMP}$)	0.6	6
Bolometric luminosity ($L_{\rm bol}$) [$L_\odot$]	1.0 ± 0.3	1
Central luminosity ($L_{\rm central}$) [$L_\odot$]	<0.1	5
Diameter (D) [× 1000 au]	∼17.8	4
Central mass[d] (M_{120}) [$M_\odot$]	$0.4^{+0.8}_{-0.3}$	1
Total mass ($M_{\rm tot}$) [$M_\odot$]	2.7 ± 0.7	2
H_2 column (N_{H_2}) [10^{22} cm^{-2}]	6–13	3,5

[a]Bonner–Ebert sphere.
[b]Power law of the form $n(r) = n_0(r_0/r)^m$.
[c]ISRF strength relative to standard MMP.
[d]In a 120-arcsec diameter beam.
[1]Shirley et al. (2000).
[2]Evans et al. (2001).
[3]Ward-Thompson et al. (1999).
[4]Bacmann et al. (2000).
[5]Ward-Thompson et al. (2002).
[6]Young et al. (2003).

The data above were analysed in detail in the presenting papers in order to constrain the structure and conditions associated with L1544. While these approaches were semi-analytic in nature and/or assumed spherical symmetry, they represent the norm in analysing long-wavelength emission from dust. Consequently, these results provide a useful first-order approximation to the underlying source conditions, and are presented in Table 2.

3 MODEL

We have constructed detailed, self-consistent, three-dimensional radiative transfer models through dust. The model utilizes a Monte Carlo approach combined with an approximate lambda iteration to ensure true convergence even at high optical depths. The model has been tested against existing 1D (Egan, Leung & Spagna 1988) and 2D (Spagna, Leung & Egan 1991) codes with good success.

Based upon the input parameters discussed below, we solve for the dust temperature and radiation field at each point in the model cloud with a typical resolution of $\sim 10^{15}$ cm. The emergent radiation, after subtraction of the background interstellar radiation field (ISRF), is then convolved with the appropriate telescope beam (Shirley et al. 2000) for comparison with observations. We do not simulate the chopping, as the chop direction and size varied with time during the observations. Evans et al. (2001) found that chopping affected the radial profile in the outer regions and were unable to determine an outer radius. While we will give an outer radius in this paper, it should be interpreted with caution. We have simulated the contours only out to radii that are not strongly affected by chopping, so conclusions about the shape of the density profile to that point should be safe. The approach of simulating the observations has the advantage that we can directly compare models to observational output, while minimizing the need for imposing outside approximations/assumptions to the observational data.

3.1 Input data

We adopt a triaxial ellipsoidal density structure for our cloud models, of the form

$$n(x, y, z) = n_0 \left[\sqrt{\frac{x^2}{a^2} + \frac{y^2}{b^2} + \frac{z^2}{c^2}} \right]^{-m}, \quad (1)$$

where n is the number density, n_0 is the reference density, (x, y, z) defines the position, (a, b, c) are parameters specifying the shape of the ellipsoid, and m is the dust density distribution exponent discussed in the following subsection. This form is consistent with the fact that the observed distribution of projected axial ratios is well matched by randomly oriented, intrinsically prolate cores (Myers et al. 1991; Ryden 1996). It is also consistent with the non-axisymmetric evolution of magnetically subcritical cores (Nakamura & Li 2002). We follow this work and the symmetry in the north-west–south-east direction, and reduce our density structure to a prolate spheroid having the long (x) axis in the north-west–south-east direction, and being symmetric in the y- and z-directions. In this case, we take $b = c$, and define the axis ratio to be $q \equiv a/b$. Based upon the observed isophotes, we consider axis ratios in the range $1.2 < q < 5$.

We assume that the dust density follows a power law, with exponent m. This significantly simplifies the source parametrization while maintaining the ability to consider various amounts of central condensation. The power-law parametrization is commensurate with similar spherical models, as the spherical average density distribution for any ellipsoid given by equation (1) is $n_{\rm spherical} \propto r^{-m}$, and is given by $n_{\rm spherical}(r) = \int \mathrm{d}\Omega\, n(x, y, z) / \int \mathrm{d}\Omega = n_0 C(a, b, c, m) r^{-m}$, where $C(a, b, c, m)$ is a constant that depends only upon the geometry, and the density distribution. Furthermore, this approach is consistent with both observations (e.g. Evans et al. 2001) and theoretical (e.g. Ciolek & Basu 2000; Curry & Stahler 2001; Nakamura & Li 2002) models of evolution of magnetized clouds. Based upon previous spherical models, we consider density distribution exponents in the range $1.0 < m < 3.0$.

The outer radius is the distance along the long (x) axis at which the cloud structure terminates, and is half of the adopted long-axis diameter, D. At this point, the cloud is presumed to mesh with the surrounding, more diffuse, medium. We consider diameters in the range $0.06 < D(\mathrm{pc}) < 0.2$ [$12\,000 < D(\mathrm{au}) < 40\,000$]. The inner radius, defined as the distance from the centre of the model space to the edge of the first non-central cell, is $r_{\rm in} \sim 0.008 \times D$.

The ISRF is the primary heat source for the grains in most of our models. We adopt the ISRF compiled by Mathis et al. (1983; hereafter MMP). The strength of the ISRF, $G_{\rm MMP} \equiv$ (adopted ISRF)/(MMP ISRF), is in the range $0.3 < G_{\rm MMP} < 3.0$. We also include the potential effects of a luminous central source by considering $10^{-6} < L_*(\mathrm{L}_\odot) < 10^{-2}$.

The absolute dust density (or mass) is constrained by the optical depth to source centre along the long axis via the optical depth at 450 μm, namely $\tau_{450} = \int n(x) \langle Q(450\ \mu\mathrm{m}) \pi a^2 \rangle\, \mathrm{d}x$. Here $n(x)$ is the number density specified above, Q is the grain absorption efficiency at 450 μm discussed below, and a is the grain radius taken to be 0.1 μm. Since the grains are small compared to the wavelength of the majority of the incident and re-emitted radiation (having $\lambda > 1$ μm), the grain opacity per unit mass is independent of the grain size (Ossenkopf & Henning 1994). Test models with different grain sizes confirm this independence of our results with adopted grain size. Finally, we consider optical depths in the range $0.01 < \tau_{450,\rm long} < 0.5$.

We adopt the dust opacities in column 5 of table 1 of Ossenkopf & Henning (1994). They have been successful in fitting observations of both high-mass (e.g. van der Tak et al. 1999, 2000; Mueller et al. 2002) and low-mass (e.g. Evans et al. 2001) star-forming regions. These opacities are calculated for grains grown by coagulation and accretion of thin ice mantles for 10^5 yr at a density of 10^6 cm^{-3}. These conditions should be applicable to the cold, dense cloud core of L1544.

3.2 Grid of models

A guided search of parameter space yielded a preliminary best-fitting (base) model as judged by the χ^2 deviation between the model and observations (see Section 4). In order to confirm the best fit, a relatively fine grid of over 400 models was constructed surrounding this best-fitting model to test the quality of fit and the geometry of the parameter space. From the base model, subgrids were constructed by varying pairs of parameters: amount and distribution of dust (τ, m), the strength of heat sources ($G_{\rm MMP}$, L_*), and the source geometry (D, q). A best-fitting model from these subgrids was identified as the new base model. The process was iterated multiple times to ensure the best fit was found. A final grid was then made surrounding the best-fitting model, with the comparison to observations discussed in Section 4.

4 COMPARISON WITH OBSERVATIONS

In order to compare the model predictions with observations, the simulated and observed data were fitted using the reduced χ^2 statistic. For the 450- and 850-μm sky maps, the major and minor axes of the isophote contours were compared, such that

$$\chi^2_{450} = \frac{1}{3} \sum_{i=1}^{2} \sum_{j=1}^{2} \left[\frac{(r_{450,i,j,\rm obs} - r_{450,i,j,\rm model})^2}{\sigma^2_{450,i,j}} \right], \quad (2)$$

and

$$\chi^2_{850} = \frac{1}{11} \sum_{i=1}^{6} \sum_{j=1}^{2} \left[\frac{(r_{850,i,j,\rm obs} - r_{850,i,j,\rm model})^2}{\sigma^2_{850,i,j}} \right]. \quad (3)$$

Here i corresponds to the number of the contour level, j corresponds to the axis (major, minor), r is the radius of the ith contour along the jth axis, σ is the uncertainty in the radius, and the leading fraction denotes the $1/(N - 1)$ term with $N_{450} = 4$ and $N_{850} = 12$ surface brightness contour data points (major and minor axes for each contour). The quality of the fit of the SED is measured similarly, via

$$\chi^2_{\rm SED} = \frac{1}{5} \sum_{k=1}^{6} \frac{(F_{k,\rm obs} - F_{k,\rm model})^2}{\sigma^2_k}. \quad (4)$$

Here k specifies the flux data point, F_k is the flux of the kth data point, σ_k is the uncertainty in that flux, and the leading 1/5 denotes the $1/(N - 1)$ term with $N_{\rm SED} = 6$ flux data points. The observed data are taken from Table 1.

The overall quality of fit was then taken from the average of the three reduced χ^2's (assuming that the 450-μm, 850-μm, and SED results are independent) as

$$\chi^2_{\rm tot} = \left(\chi^2_{450} + \chi^2_{850} + \chi^2_{\rm SED} \right) / 3. \quad (5)$$

This choice for overall fit quality is advantaged by the fact that in general none of the individual χ^2's dominate the others for good fits. Furthermore, the individual χ^2's are potentially more sensitive to

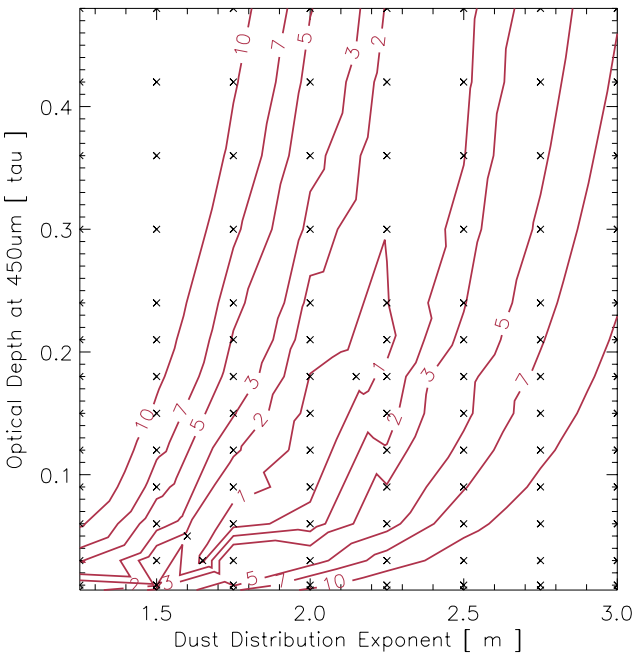

Figure 1. Contours of χ^2 fit for the models in the τ_{450}–m plane. Note that while there is some degeneracy, the region is limited, enabling a constraint to be placed on both τ_{450}, and m.

different parameters. For example, the SED is dependent on the dust mass (e.g. Hildebrand 1983; Doty & Leung 1994), while the surface brightness is more dependent upon the density and temperature distribution (e.g. Doty & Palotti 2002; Shirley, Evans & Rawlings 2002). As a result, the fit to $\chi^2_{\rm tot}$ requires a simultaneously strong fit to all data. Unless otherwise noted, it is this value of χ^2's that is discussed below. For reference, our best-fitting model has $\chi^2_{\rm tot} = 0.5$.

4.1 Optical depth and density distribution

The amount of dust and its distribution can be parametrized by τ and m. In Fig. 1, we plot χ^2 contours for a grid of models in the τ_{450}–m plane. The models run are denoted by the crosses. There exists a slight degeneracy between τ_{450} and m, in that a range of models yields $\chi^2 < 1$. This is similar to the degeneracy in the τ–m parameter space found by Doty & Palotti (2002) when fitting the SEDs of spherical models. However, in this case, the spatial distribution of intensity (i.e. the sky maps) allow the degeneracy to be more nearly broken.

Based upon these results, we infer that the optical depth at 450 μm can be constrained to $0.06 < \tau_{450,\rm long} < 0.24$. These values are, however, defined along the long axis of the ellipsoid. The optical depth along the short axis is a factor of ∼4 lower, or in the range $0.015 < \tau_{450,\rm short} < 0.06$. This corresponds to optical depths of $2 \times 10^{-3} < \tau_{1300,\rm short} < 8 \times 10^{-3}$ at 1300 μm, and $0.06 < \tau_{200,\rm short} < 0.24$ at 200 μm. These ranges are consistent with those of previous observations and spherical modelling. This is to be somewhat expected, as at these wavelengths the source is transparent, so that nearly all grains can be seen. As a result, the total amount of energy absorbed from the ISRF plays a slightly larger role than the spatial symmetry, meaning that the spherical model 'average optical depth' is an appropriate starting point.

The results of Fig. 1 also suggest that the dust density distribution can be well fitted by a power law of the form in equation (1), with an exponent $1.75 < m < 2.25$. This is generally consistent with the previous results from spherical modelling which suggest that a power law having $m = 2$ would fit the data (Evans et al. 2001), so long as a self-consistent temperature distribution is adopted. Again, this is somewhat expected, as the density power law can be viewed as essentially fixing the relative amounts of 'warm' outer dust to 'cold' inner dust. Consequently, for a relatively regular source which is transparent at the wavelengths of interest, it appears that the spherical average density distribution provide a reasonable first-order estimate. Most strikingly, when a self-consistent, depth-dependent temperature distribution, and the source asphericity are taken into account, the data are well fitted by a singular power-law density distribution.

In order to probe the ability of a Bonner–Ebert-like density power law to fit the observations, we have also considered models with a flattened density distribution within a sphere of radius $r_{\rm cut}$. When we allow the density distribution for $r > r_{\rm cut}$ to vary (keeping m and τ_{450} constant), we find that a central flattening for $r < 0.002$ pc $= 400$ au will produce adequate fits. On the other hand, when the density profile is unchanged for $r > r_{\rm cut}$ (allowing τ_{450} to vary), acceptable fits are found for $r_{\rm cut} < 0.008$ pc $= 1600$ au. This is roughly consistent with the results of Evans et al. (2001) in the sense that our density at 1600 au is $\sim 10^6$ cm^{-3}, the same as the central density for their best-fitting BE sphere. In order to place $r_{\rm cut} < 1600$ au in context, we note that the size of the ∼15-arcsec beam at 850 μm is ∼0.01 pc = 2000 au. As a result, while we cannot rule out a flattened Bonner–Ebert-like central density distribution, it is restricted to $r < 1600$ au, and is essentially unresolved at the resolution limit of the observations.

The best-fitting density distribution and spherical comparators are given in Fig. 2. The solid and dotted lines are the best-fitting power-law and Bonner–Ebert spherical density profiles from Evans et al. (2001). The long-dashed line is the spherical average of our best-fitting ellipsoidal profile (see Section 3.1). Notice that, in general,

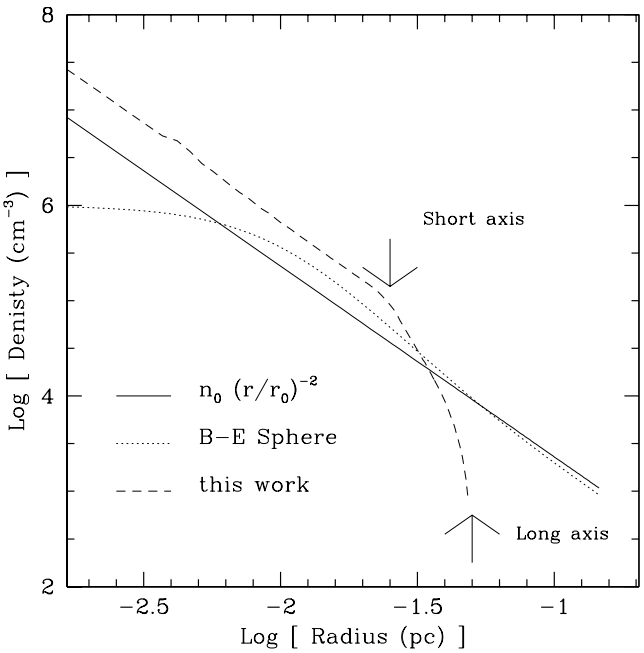

Figure 2. Density profiles for L1544. The spherical average of the best-fitting ellipsoidal distribution is given by the long-dashed lines. Also plotted are the corresponding best-fitting Bonner–Ebert sphere (dotted line) and spherical power law (solid line) from Evans et al. (2001).

our best-fitting model represents a denser, smaller cloud than the previous spherical modelling. Furthermore, our best-fitting model maintains an $m = 2$ profile, for $r < R_{\rm short}$. However, once $r > R_{\rm short}$, the spherical average density falls much faster with $m \sim 4$–5 due to the averaging of high-density on-cloud and low-density off-cloud positions in taking the spherical average. Interestingly, this steep density fall-off is consistent with the results of Abergel et al. (1996) and Bacmann et al. (2000), even though along any given ray from the centre of the cloud, $m = 2$.

Finally, we note that our temperature distribution is roughly consistent with the self-consistent spherical modelling of Evans et al. (2001), and the analytic work of Zucconi, Walmsley & Galli (2001) for L1544. In particular, we find an unattenuated (outer) spherical average dust temperature of ∼15 K, in keeping with the work of Zucconi et al. (2001), and an inner spherical average temperature of ∼5.4 K. The inner temperature is consistent with the Zucconi results for a high central density ($n_{\rm H} = 4.4 \times 10^6$ cm^{-3}), but approximately 2 K lower than the Evans et al. (2001) and Zucconi et al. (2001) results for the power-law density distribution adopted here. This has two causes. First, the central density for our power-law model is closer to that of Zucconi et al. (2001). Also, while our short axis is only slightly more opaque than the spherical models of Evans et al. (2001), our long axis is more opaque by a factor of ∼2. The increased opacity leads to less radiation penetration, and thus lower temperatures in our models.

4.2 ISRF and central luminosity

The strength of the external and internal heat sources are parametrized by $G_{\rm MMP}$ and L_*. In Fig. 3, we plot the χ^2 contours in the $G_{\rm MMP}$–L_* plane. Again, the crosses signify the models considered. In this case, we can see that there is no degeneracy between these two parameters (similar to results for fitting SEDs, Lis et al. 2001). This is due to the fact that the size and spacing of the outer contours is mostly determined by the external heat source (the ISRF), while the inner contours are determined by the opacity at the wavelength of the dominant heating radiation and the luminosity of the central source. Consequently, each parameter probes a different region of the spatial intensity distribution maps.

Based upon the results of Fig. 3, we can constrain the strength of the external heat source, namely the ISRF, to be $0.8 < G_{\rm MMP} < 1.6$. This is significant in that while it is consistent with the MMP ISRF, it is approximately a factor of 1.5–3 larger than the reduced field used by Evans et al. (2001), and the attenuated field adopted by Young et al. (2004) in their spherical modelling. This difference is due to the fact that for wavelengths which dominate the absorbed radiation ($\lambda < 25$ μm), the spherical clouds are effectively larger (more optical depth at larger radii). Thus, the stronger radiation field found here is consistent with the smaller surface area, mass, and higher optical depth in our model versus the equivalent spherical modelling.

Last, it is useful to note that we have considered the $G_{\rm MMP}$–D plane of fits, finding that $G_{\rm MMP}$ is relatively unaffected due to the small optical depth of the models. Together with the discussion above, this result points to the potential to infer local conditions when modelling combined spectral and spatial data.

Of perhaps even greater interest, it is also possible to constrain the central luminosity. We find $L_* < 10^{-3}$ L$_\odot$. This result is commensurate with the fact that no IRAS source exists at this position (Beichman et al. 1986), and with the assignation of this source as a pre-protostellar object (Ward-Thompson et al. 1994). The dominant factor in constraining the luminosity is the surface brightness distribution. For the source mass and optical depth, a central source of luminosity $L > 10^{-3}$ L$_\odot$ yields a relatively strong point source in the maps, and a concomitant decrease in the size and ellipticity of the intensity contours.

The luminosity constraint at first appears inconsistent with the central luminosity quoted in Table 1. However, the limit in Table 1 arises from the difference between the incident luminosity from the ISRF (∼0.1 L$_\odot$) and the emergent luminosity (∼0.2 L$_\odot$) found by

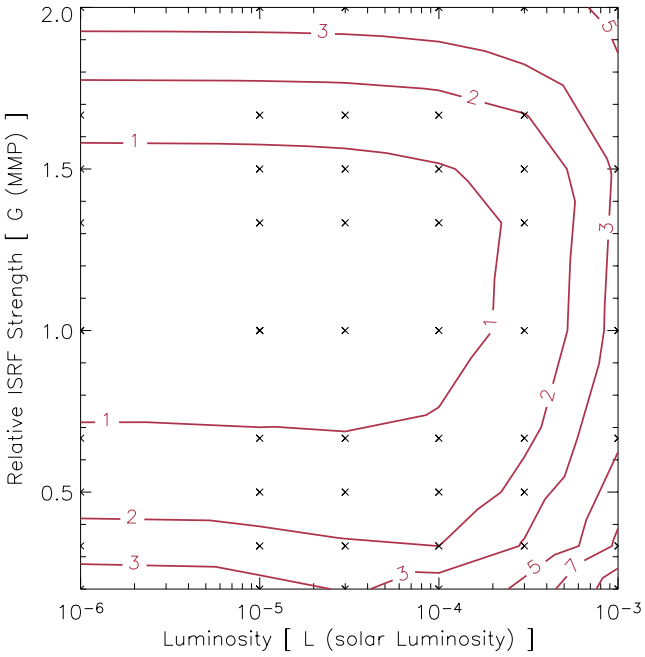

Figure 3. Contours of χ^2 fit in the ISRF–L_* plane. Note that there is no degeneracy between the parameters, and that significant limits can be set.

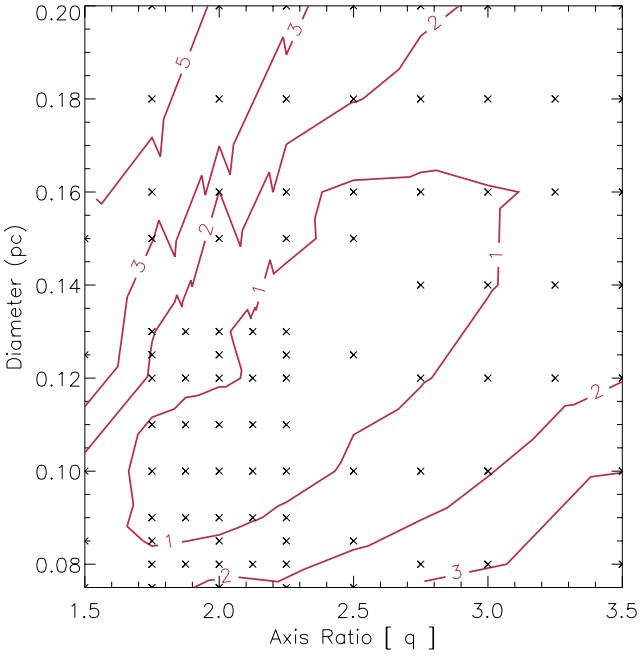

Figure 4. Contours of χ^2 fit for models in the D–q plane. Note that while there is a degeneracy, it is limited so that constraints can be placed on these parameters.

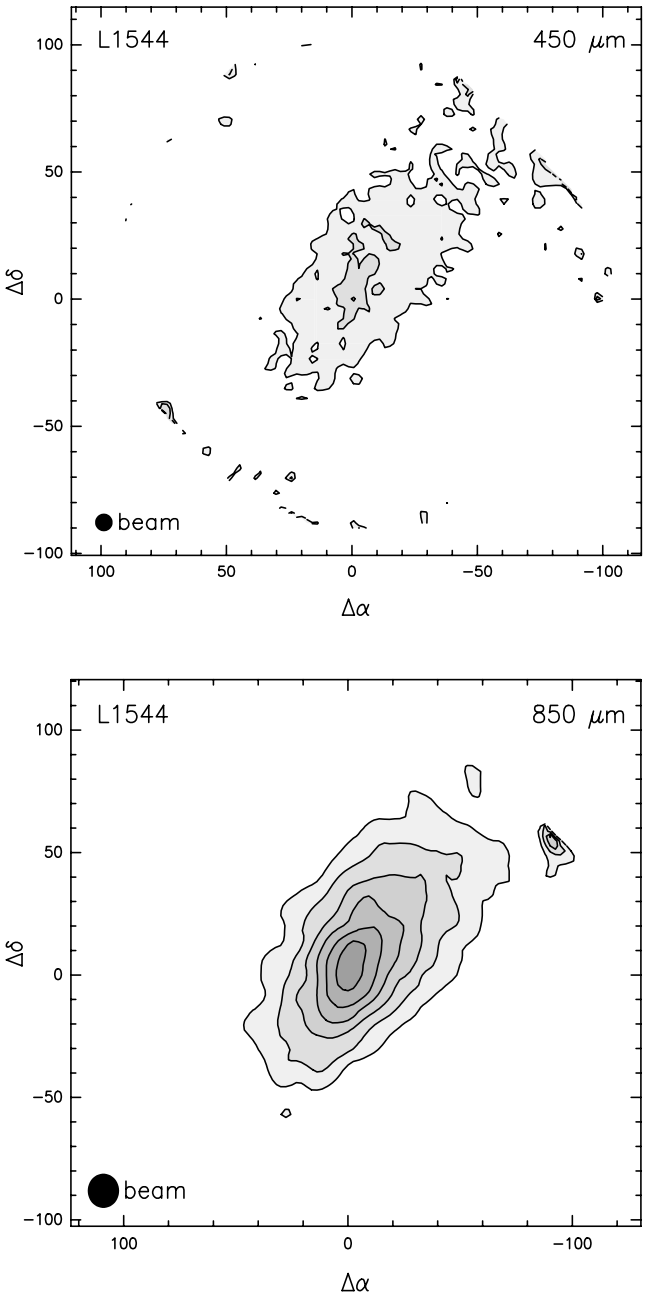

Figure 5. Intensity contours for L1544. Top panel: 450 μm; lowest contour level at 50 per cent of peak flux (3σ), with levels increasing by 33 per cent. Lower panel: 850 μm; lowest contour level at 20 per cent of peak flux (3σ), with levels increasing by 13 per cent. Data from Shirley et al. (2000).

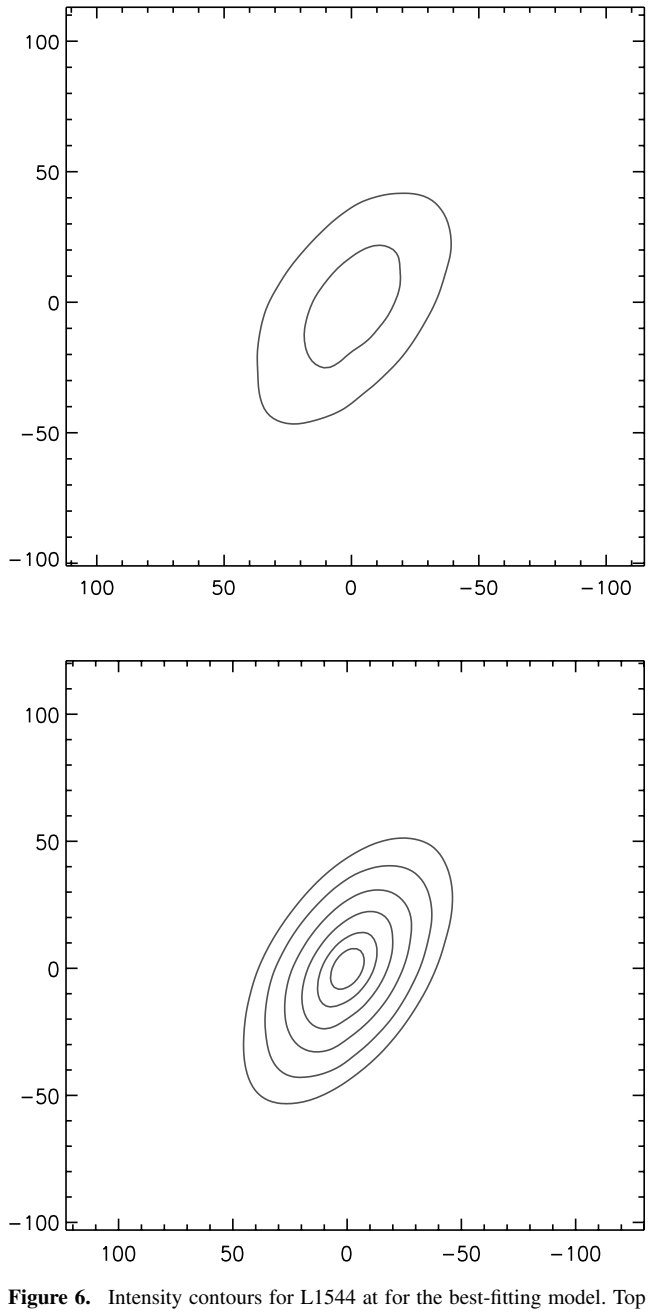

Figure 6. Intensity contours for L1544 at for the best-fitting model. Top panel: 450 μm. Lower panel: 850 μm. The contour levels are the same as in Fig. 5.

Ward-Thompson et al. (2002). As discussed by those authors, the small difference suggests that $L_{\rm central} \sim 0$ may well be within the uncertainties in their analysis. Consequently, the work here provides a much more strenuous constraint on the upper limit to the luminosity of any central source. Furthermore, while there may be infall (Tafalla et al. 1998; Williams et al. 1999), the low luminosity inferred here confirms the previous result that the collapse is nearly isothermal with a correspondingly small compressional luminosity (Henriksen 1994), and is inconsistent with the formation of a luminous protostar at the centre of the collapsing core.

4.3 Outer diameter and axis ratio

The size and shape of the cloud are parametrized by D and q. The χ^2 contours for the diameter (D)–axis-ratio (q) plane are shown in Fig. 4. While there is some degeneracy between the diameter and axis ratio, it is again limited. In this case, the degeneracy is limited by the fact that the flux and hence the SED is more sensitive to the outer diameter, while the spatial intensity contours are sensitive to both the axis ratio and the diameter.

Based upon the results in Fig. 4, the outer diameter of the long axis of the source can be constrained to $0.08 < D({\rm pc}) < 0.16$ [$16\,000 < D({\rm au}) < 32\,000$]. This is consistent with the size inferred by Bacmann et al. (2000). It is, however, smaller than the diameter adopted in the spherical modelling of Evans et al. (2001), who

adopted an arbitrarily large diameter to simulate chopping into an extended cloud. It should be noted that the actual cloud size may be somewhat larger than the value inferred here as discussed in Section 3.

It is also possible to constrain the axis ratio of the source. We find $1.7 < q < 2.5$. This is roughly consistent with the isophotes for the 450- and 850-μm sky maps, which show axis ratios in the range 1.5–4. The observed axis ratios are large because the external heating radiation must travel a longer physical distance along the short axis than along the long axis to reach the same optical depth. As a result, isophotes are more elongated than the underlying isodensity contours.

4.4 Comparison of best-fitting model with observations

Based upon the results above, our best-fitting model for L1544 is a prolate spheroid having an axis ratio of $q = 2$, with an ellipsoidal power-law density distribution given by equation (1) having $m = 2$. We infer the optical depth along the long axis at 450 μm to be $\tau_{450} = 0.12$, and the central luminosity to be $L_* = 0$. Finally, we infer that an unscaled MMP ISRF, and an outer diameter along the long axis of $D = 0.1$ pc $= 20\,000$ au (though it could be somewhat larger), provide a best fit to the data.

A comparison of the 450- and 850-μm sky maps with the best-fitting model is shown in Figs. 5 and 6. Notice that the fits are generally quite good, in terms of the size and width of the intensity contours. For comparison, Fig. 7 gives similar sky-map intensity contours for representative models with $\chi^2_{\rm tot} = 2$ (solid lines), and $\chi^2_{\rm tot} = 5$ (broken lines), respectively. The contour levels are the same as in Fig. 5. Notice that the sky maps for even these somewhat low values of $\chi^2_{\rm tot}$ are significantly worse than for the best-fitting model(s).

Likewise, the observed and modelled SEDs are compared in Fig. 8. The observational data (symbols with error bars) are taken from Table 1. The solid line corresponds to the best-fitting model, while the dotted and dashed lines correspond to the $\chi^2_{\rm tot} = 2, 5$ models discussed above, respectively. As before, the best-fitting model reproduces the observed data well. On the other hand, although the $\chi^2_{\rm tot} = 5$ model is well outside the observed SED limits, the same is not true for the $\chi^2_{\rm tot} = 2$ model. While the $\chi^2_{\rm tot} = 2$ model is at the very limits of acceptability, it is still consistent with the observed SED. This is in keeping with the result of Doty & Palotti (2002) that fitting the SED alone can yield degenerate solutions (see also, e.g. Men'shcikov & Henning 1997; Lis et al. 2001). Furthermore, it underlines the significance of resolving the source, and simultaneously fitting both the surface brightness and SED to best constrain the source properties.

Finally, the inferred ranges and best-fitting values for the parameters specifying the structure and conditions of L1544 are summarized in Table 3, along with values inferred from previous work. As noted previously, we see that conclusions from earlier modelling of observations at wavelengths for which the source is optically thin yield results which are relatively close to the best-fitting models. Even more interesting is the fact that under the same conditions, spherical models yield results which are reasonable first-order approximations. Still, it should be noted that even in the simple case of a centrally condensed, externally heated, optically thin, ellipsoidal power-law density distribution with an axis ratio of ∼2, geometrical and radiative transfer effects do cause deviations from results inferred from simpler analyses. As a result, self-consistent, multi-dimensional modelling is an important tool for understanding radiation from aspherical sources.

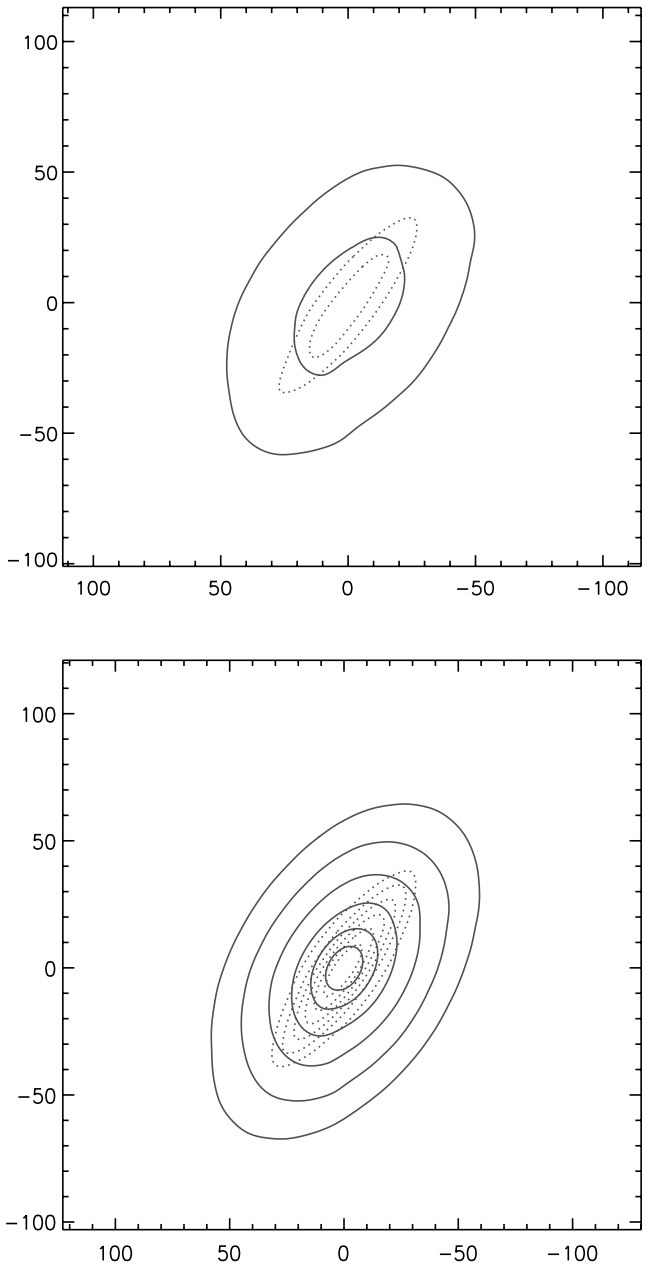

Figure 7. Model intensity contours for L1544 at 450 μm (top panel) and 850 μm (bottom panel) for a representative model having $\chi^2_{\rm tot} = 2$ (solid lines) and $\chi^2_{\rm tot} = 5$ (dotted lines). The contour levels are the same as those in Fig. 5.

5 CONCLUSIONS

We have constructed models for the non-spherical protostellar core L1544 utilizing a fully three-dimensional continuum radiative transfer model. After convolving the model output with the actual SCUBA beam profile, we are able to compare our results with existing observations, including both SEDs and sky maps. Based upon this work, we find that:

(i) It is possible to constrain the optical depth and density distribution. While a degeneracy in this plane exists as noted by Doty & Palotti (2002), the spatial intensity distribution more nearly breaks the degeneracy. In particular, we find $2 \times 10^{-3} < \tau_{1300,\rm short} < 8 \times$

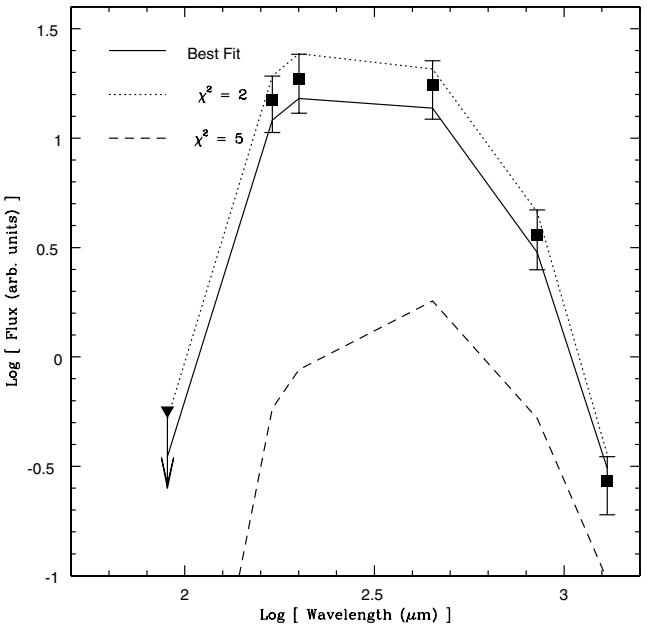

Figure 8. Comparison of the SED for the best-fitting model (solid line), a model with $\chi^2_{\rm tot} = 2$ (dotted line), $\chi^2_{\rm tot} = 5$ (dashed line), and observations (solid symbols with error bars).

Table 3. Inferred conditions for L1544.

Parameter	Previous value	This work
Optical depth (τ_{1300}) [$\times 10^{-3}$]	2	5 ± 3
Optical depth (τ_{200})	0.06	0.15 ± 0.09
Density power law (m)	2^a	2.0 ± 0.25
ISRF ($G_{\rm MMP}$)	0.6	1.0 ± 0.5
Central luminosity (L_*) [$L_\odot$]	<0.1	$<10^{-3}$
Diameter (D) [$\times$ 1000 au]	$\sim$17.8	12^b–24^c
Central mass (M^d_{120}) [$M_\odot$]	$0.4^{+0.8}_{-0.3}$	0.2 ± 0.1
Total mass ($M_{\rm tot}$) [$M_\odot$]	2.7 ± 0.7	1.4 ± 0.9
H_2 column (N_{H_2}) [10^{22} cm^{-2}]	6–13	14 ± 9

[a]Bonner–Ebert sphere or power law with $m = 2$.
[b]Diameter of short axis.
[c]Diameter of long axis.
[d]In a 120-arcsec diameter beam.

10^{-3}, and $0.06 < \tau_{200,\rm short} < 0.24$. Likewise, we find that an ellipsoidal density power law with an exponent $m \sim 2$ ($1.75 < m < 2.25$) can fit the observations well. While a Bonner–Ebert-like centrally flattened density distribution cannot be ruled out, the central flattening can be restricted to $r < 0.008$ pc $= 1600$ au (Section 4.1).

(ii) The ISRF and central luminosity are nearly orthogonal parameters. The ISRF can be constrained to be within $\sim$50 per cent of that defined by Mathis et al. (1983), somewhat higher than previously inferred from spherical modelling. The central luminosity can also be constrained to $<10^{-3}$ $L_\odot$, consistent with the assignation of this source as a pre-protostellar object (Section 4.2).

(iii) The diameter and axis ratio show a limited degeneracy, which is again broken by the spatial intensity distribution. We infer a long-axis diameter of $0.08 < D({\rm pc}) < 0.16$ [$16\,000 < D({\rm au}) < 32\,000$], and an axis ratio $1.7 < q < 2.5$. The outer diameter and axis ratio may each be somewhat larger due to potential on-source chopping in the observations, and the projection of the long axis on to the plane of the sky. Both the diameter (D) and the axis ratio (q) are less than would be inferred directly from observations, and are due to radiative transfer effects and non-spherical geometry (Section 4.3).

(iv) The values and ranges of values found here are roughly consistent with those inferred directly from observations or spherical modelling, due to the relative transparency of the source at the wavelengths of observation. In general, we infer a smaller source of lower mass and higher optical depth/column density than previously assumed (Section 4.4).

(v) The SED yields degenerate fits. A 'best-fit' requires both the SED and surface brightness distribution. This approach, combined with a large grid of models ($\sim$400), can yield a best-fit and range of uncertainty in inferred parameters. Interestingly, a range of 10 (0.5–5) or even 4 (0.5–2) in χ^2 can yield a remarkably different quality of fit (Section 4.4).

ACKNOWLEDGMENTS

We are grateful to Chad Young and Rebecca Metzler for interesting discussions. This work was partially supported under grants from The Research Corporation and the Denison University Research Foundation (SDD), NASA grants NAG5-10488 and NNG04GG24G to the University of Texas at Austin (NJE), and a Battelle Intership (MLP).

REFERENCES

Abergel A. et al., 1996, A&A, 315, L329
Adams F. C., 1991, ApJ, 382, 544
André P., Ward-Thompson D., Motte F., 1996, A&A, 314, 625
Bacmann A., André P., Puget J.-L., Abergel A., Bontemps S., Ward-Thompson D., 2000, A&A, 361, 555
Beichman C. A., Myers P. C., Emerson J. P., Harris S., Mathieu R., Benson P. J., Jennings R. E., 1986, ApJ, 307, 337
Benson P. J., Myers P. C., 1989, ApJS, 71, 89
Butner H. M., Evans N. J., II, Lester D. F., Levreault R. M., Strom S. E., 1991, ApJ, 376, 636
Ciolek G. E., Basu S., 2000, ApJ, 529, 925
Curry C. L., Stahler S. W., 2001, ApJ, 555, 160
Doty S. D., Leung C. M., 1994, ApJ, 424, 729
Doty S. D., Palotti M. L., 2002, MNRAS, 335, 993
Egan M. P., Leung C. M., Spagna G. F., Jr., 1988, Comput. Phys. Comm., 48, 271
Elias J. H., 1978, ApJ, 224, 857
Evans II N. J., Rawlings J. M. C., Shirley Y. L., Mundy L. G., 2001, ApJ, 557, 193
Henriksen R., 1994, in Montmerle T., Lada C. J., Mirabel I. F., Tran Than Van J., eds, The Cold Universe. Editions Frontieres, Gif-sur-Yvette, p. 241
Hildebrand R. H., 1983, QJRAS, 24, 267
Ladd E. F., Adams F. C., Fuller G. A., Myers P. C., Casey S., Davidson J. A., Harper D. A., Padman R., 1991, ApJ, 382, L555
Lis D. C., Serabyn E., Zylka R., Li Y., 2001, ApJ, 550, 761
Mathis J. S., Mezger P. G., Panagia N., 1983, A&A, 128, 212
Men'shcikov A. B., Henning Th., 1997, A&A, 318, 879
Mueller K. E., Shirley Y. L., Evans N. J., II, Jacobson H. R., 2002, ApJS, 143, 469
Myers P. C., Linke R. A., Benson P. J., 1983, ApJ, 264, 517
Myers P. C., Fuller G. A., Goodman A. A., Benson P. J., 1991, ApJ, 376, 561
Nakamura F., Li Z.-Y., 2002, ApJ, 566, L101
Ossenkopf V., Henning Th., 1994, A&A, 291, 943
Ryden B. S., 1996, ApJ, 471, 822

Shirley Y. L., Evans N. J., II, Rawlings J. M. C., 2002, ApJ, 575, 337
Shirley Y. L., Evans N. J., II, Rawlings J. C., Gregersen E. M., 2000, ApJS, 131, 249
Spagna G. F., Jr, Leung C. M., Egan M. P., 1991, ApJ, 379, 232
Tafalla M., Mardones D., Myers P. C., Caselli P., Bachiller R., Benson P. J., 1998, ApJ, 504, 900
van der Tak F. F. S., van Dishoeck E. F., Evans N. J., II, Bakker E. J., Blake G. A., 1999, ApJ, 522, 991
van der Tak F. F. S., van Dishoeck E. F., Evans N. J., II, Blake G. A., 2000, ApJ, 537, 283
Ward-Thompson D., André P., Kirk J. M., 2002, MNRAS, 329, 257
Ward-Thompson D., Motte F., André P., 1999, MNRAS, 305, 143
Ward-Thompson D., Scott P. F., Hills R. E., André P., 1994, MNRAS, 268, 276
Williams J. P., Myers P. C., Wilner D. J., di Francesco J., 1999, ApJ, 513, L61
Young C. H., Shirley Y. L., Evans N. J., Rawlings J. M. C., 2003, ApJS, 145, 111
Young K. E., Lee J.-E., Evans II N. J., Goldsmith P. F., Doty S. D., 2004, ApJ, 614, 252
Zucconi A., Walmsley C. M., Galli D., 2001, A&A, 650, 662

This paper has been typeset from a TEX/LATEX file prepared by the author.